Research Square

Preprints are preliminary reports that have not undergone peer review.
They should not be considered conclusive, used to inform clinical practice,
or referenced by the media as validated information.

Anti-Kasha fluorescence, persistent room-temperature phosphorescence and delayed emission from a nearly flat non-symmetric polycyclic hydrocarbon

Eduard Westphal

eduard.w@ufsc.br

Federal University of Santa Catarina https://orcid.org/0000-0002-5711-5365

Monike Kutz

Federal University of Santa Catarina

Carolina Francener

Durham University

Wataru Ota

Kyoto University

Manuela Corrêa

Federal University of Santa Catarina

Daniel Crane

Durham University https://orcid.org/0009-0009-7777-7583

Emiko Fujiwara

Kyoto University

Tohru Sato

Kyoto University

Ivan Bechtold

Universidade Federal de Santa Catarina

Andrew Monkman

Durham University https://orcid.org/0000-0002-0784-8640

Harald Bock

Centre National de la Recherche Scientifique

Article

Keywords:

Posted Date: June 16th, 2026

DOI: https://doi.org/10.21203/rs.3.rs-9960552/v1

License: This work is licensed under a Creative Commons Attribution 4.0 International License.
Read Full License

Additional Declarations: There is **NO** Competing Interest.

Version of Record: A version of this preprint was published at Nature Communications on October 2nd, 2026. See the published version at https://doi.org/10.1038/s41467-026-78107-6.

Anti-Kasha fluorescence, persistent room-temperature phosphorescence and delayed emission from a nearly flat non-symmetric polycyclic hydrocarbon

Monike da Silva Kutz[a,b†], Carolina Francener[c†], Wataru Ota[d,e], Manuela Santos Corrêa[a], Daniel Crane[c], Emiko Fujiwara[d], Tohru Sato[d,e$], Ivan H. Bechtold[f], Andrew P. Monkman[c#], Eduard Westphal[a*], Harald Bock[b]

[a] *Department of Chemistry, Universidade Federal de Santa Catarina, Florianópolis, Brazil*

[b] *Centre de Recherche Paul Pascal, Université de Bordeaux/Centre National de la Recherche Scientifique, Pessac, France*

[c] *Department of Physics, Durham University, Durham, United Kingdom*

[d] *Fukui Institute for Fundamental Chemistry, Kyoto University, Takano Nishibirakicho 34-4, Sakyo-ku, Kyoto 606-8103, Japan*

[e] *Department of Molecular Engineering, Graduate School of Engineering, Kyoto University, Nishikyo-ku, Kyoto 615-8510, Japan*

[f] *Department of Physics, Universidade Federal de Santa Catarina, Florianópolis, Brazil*

$ Corresponding author: tsato@scl.kyoto-u.ac.jp
 # Corresponding author: a.p.monkman@durham.ac.uk
** Corresponding author: eduard.w@ufsc.br*
[†] These authors contributed equally to this work

Abstract

We introduce monohomotruxene (**MHTX**), a non-symmetric polycyclic aromatic hydrocarbon (PAH) designed by reducing the symmetry of homotruxene (**HTX**) and truxene (**TX**). This partial planarization greatly enhances the complex photophysics over symmetric, triply twisted **HTX**, substantially increasing the photoluminescence quantum yield (PLQY) in both solution and solid state, a result we attribute to its enhanced molecular rigidity and symmetry breaking. **MHTX** displays an unconventional violation of Kasha's rule, yielding excitation-dependent dual emission, giving a greater total PLQY than measured when exciting S_1. Excitation of the S_2 state under anaerobic conditions produces intense, 455-480 nm, ultralong room-temperature phosphorescence (RTP), lasting over 12 s at room temperature, the longest phosphorescence reported for a hydrocarbon. In contrast, excitation to the S_1 state yields prompt fluorescence and weak delayed fluorescence (DF) by triplet-triplet annihilation (TTA) in the neat film. Aggregate species also present a complex emissive behavior with weak orange phosphorescence and strong, blue TTA-DF. These findings establish **MHTX** as a highly promising new emissive scaffold, highlighting the remarkable potential of non-symmetric PAH architectures for accessing complex excited-state dynamics and advanced photophysical functionalities.

Introduction

Persistent room-temperature phosphorescence (pRTP), is the long-lived emission originating from a triplet excited state that remains visible to the naked eye for a period ranging from seconds to tens of hours[1,2]. Materials that show it are useful in security printing[3,4], information storage[5], time-gated biological imaging[6,7], and oxygen sensors[8]. Currently, the majority of organic pRTP emitters are heavy metal-containing molecules, where charge-transfer (CT) processes mix singlet (S_n) and triplet (T_n) excitons, and the strong spin–orbit coupling (SOC) improves both the rate of intersystem crossing (ISC) (k_{ISC}) and phosphorescence (k_{Ph})[9].

However, metal-based phosphors, such as metal-organic complexes, are often toxic, expensive, chemically unstable, poorly soluble and difficult to process[10,11]. To overcome these limitations, recent efforts have focused on the molecular design of purely organic pRTP emitters, whose structural versatility is exploited to achieve efficient metal-free RTP[12,13].

One common molecular design strategy to increase triplet excited state yield after photoexcitation focuses on enhancing the k_{ISC} to outcompete both the fluorescence (k_f) and the internal conversion (k_{IC}) rate[14]. This includes: (i) employing the heavy-atom effect (HAE) by incorporating halogen atoms (Cl, Br, I) to enhance SOC[15–17]; (ii) promoting charge-transfer (CT) character to satisfy El-Sayed's rule, either by introducing carbonyl groups[18] or heteroatoms with lone electron pairs (*e.g.*, O, N, S); and (iii) minimizing the singlet-triplet energy gap (ΔE_{ST}) using twisted donor-acceptor (D-A) architectures, which facilitates the mix of S_n and T_n states, in accordance with El Sayed's law[19–21]. Additionally, ISC restrictions can be lifted through spin-vibronic coupling vie out-of-plane modes[22].

Further, to achieve pRTP, the spin-forbidden nature of radiative triplet decay in heavy-atom-free and metal-free molecules is important. The primary challenge in these systems is not just enabling intersystem crossing (ISC), but outcompeting efficient non-radiative decays. This is addressed by designing rigid molecular structures that suppress higher-amplitude vibrational motions in the T_1[23]. In planar and symmetric aromatics systems, ISC can be efficient even without heavy atoms if a higher-energy triplet state (T_n) is close to S_n. However, an enhancement of k_{ISC} might also lead to greater phosphorescence rate (k_{ph}), diminishing its persistence. One alternative is to utilize different excited states, enabling efficient ISC through upper states while maintaining slow radiative decay between T_1 and S_0.

Homotruxene (**HTX**; Figure 1a), a non-planar C_3-symmetric twisted polycyclic aromatic hydrocarbon (PAH), displays blue delayed fluorescence (DF) by triplet-triplet annihilation (TTA) and persistent RTP from aggregate species. The orange aggregate RTP, whose phosphorescence lifetime (τ_{Ph}) was determined to be 0.38 s, can be easily observed by the naked eye when **HTX** powder is excited at 365 nm[24]. High triplet-state generation in **HTX** is due to an efficient ISC promoted by out of plane vibronic coupling SOC from torsional strain between the molecular orbitals. As the initial (π) and final excited states (π^*) are twisted, the change in orbital angular momentum upon excitation, or de-excitation, results in a non-zero spin-orbit coupling matrix element (SOCME), enabling triplet-state population[16,21]. However, truxene (**TX**; Figure 1a), the planar analogue, does not show any aggregate RTP in the solid state when excited at 365 nm[24].

In this work, we demonstrate how enhancing molecular planarity and rigidity, and reducing the symmetry from **HTX** can preserve TTA and RTP, enhance the photoluminescence quantum yield (PLQY) and result in complex photophysics. For this, we replaced two of the three flexible non-planar six-membered rings in **HTX** with planar five-membered rings, resulting in a non-symmetric nearly-flat polycyclic aromatic hydrocarbon (PAH), dubbed monohomotruxene (**MHTX**; Figure 1a). This modification was designed to reduce non-radiative vibrational decay by increasing rigidity, and to verify the limits of planarization of **HTX** to retain its optical properties. Furthermore, by leveraging the innate torsion of the homotruxene core, we aimed to enhance spin-orbit coupling (SOC) without introducing heteroatoms for lone-pair donation. In this case SOC could be promoted via out-of plane vibrational coupling, but also, as in coronene, through vibrational mixing of (π,π^*) and (σ, π^*) orbitals[25]. This mechanism can give rise to efficient ISC and radiative decay of the triplet to the ground state without the need for coupling to high energy vibronic modes. Quenching of these modes by molecular rigidity would greatly reduce non-radiative processes such as internal conversion.

Results and Discussion

Synthesis

MHTX was synthesized via a two-step route to minimize the formation of yield-compromising byproducts from the direct reaction of 1-indanone (**1**) and 1-tetralone (**3**) (Figure 1b). The first step involved the preparation and selective isolation of the α,β-unsaturated dimer (**2**) of the aldol self-condensation of 1-indanone (**1**) in the presence of titanium tetrachloride and triethylamine[26]. Subsequently, the purified dimer underwent a Brønsted acid-catalyzed aldol condensation under an argon atmosphere and in the absence of light with a four-fold molar excess of 1-tetralone (**3**) to afford **MHTX**[27]. Optimization studies (Table S1) identified as the most efficient conditions an equimolar combination of anhydrous *para*-toluenesulfonic acid (PTSA) and propionic acid (1.75 molar equivalents of each relative to **2**) as catalysts. Synthetic procedures for **MHTX**, **TX**, and **HTX**, alongside reaction optimization data and full structural characterization, are provided in the Supporting Information.

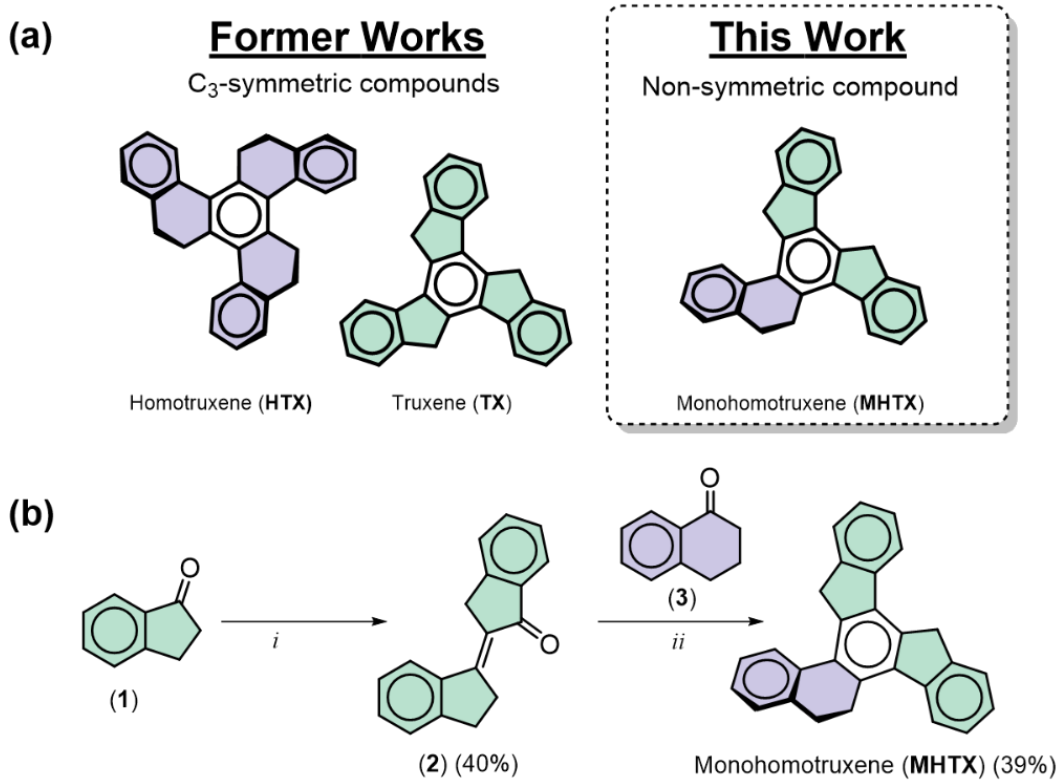


Figure 1. Structure and synthetic route of MHTX. (a) Molecular structures of homotruxene (**HTX**)[16,24], truxene (**TX**)[28] and the novel non-symmetric **MHTX** reported in this work. **(b)** Synthetic route to **MHTX**: (*i*) $TiCl_4$, triethylamine, dichloromethane, hexane, 16 hours at room temperature under argon; (*ii) para*-toluenesulfonic acid, propionic acid, *ortho*-dichlorobenzene, 24 hours at 140 °C under argon in the dark

Anti-Kasha fluorescence of MHTX

The absorption spectra were recorded in different solvents (Figure 2a and Extended Table 1). In 2-methyltetrahydrofuran (2-MeTHF; 10 µM), **MHTX** exhibits a strong absorption band with a maximum at 271 nm ($\varepsilon = 7.6 \times 10^4$ L cm^{-1} mol^{-1}) and shoulder-like features at 288 and 297 nm. In DCM (10 µM), the maximum is slightly red-shifted to 274 nm, while the shoulders remain at the same wavelengths. Moreover, the molar absorptivity in DCM is somewhat higher than in 2-MeTHF. Weaker bands ($\varepsilon < 1.4 \times 10^3$ L cm^{-1} mol^{-1}) are observed in the 315 – 380 nm range in both solvents. Upon increasing the concentration (1 mM) and in the solid state (1 wt.% in Zeonex drop-cast film; Figure S11a), the weak bands become prominent, with distinct maxima at 325, 336, 351, and 378 nm. This spectral profile is identical to the analogous C_3-symmetric compounds **HTX (**Figure S11b) and **TX (**Figure S11c)[24,29], where the intense bands are assigned to the symmetry-allowed $S_0 \rightarrow S_3$ and $S_0 \rightarrow S_4$ transitions, and the lower-intensity bands to the symmetry-allowed $S_0 \rightarrow S_2$ transition and symmetry-forbidden $S_0 \rightarrow S_1$ transition, as described in the theory section. Therefore, the degree of symmetry breaking in **MHTX** is insufficient to completely lift the symmetry selection rule, as the first two electronic transitions remain largely forbidden in character.

Unexpectedly, steady-state photoluminescence measurements reveal anti-Kasha emissive behavior for **MHTX**, as very weakly observed in coronene[30].In solution, excitation at the edge of the strong absorption region (λ_{Ex} = 300 nm) yields a vibrationally structured emission band with maxima at 350 and 360 nm and shoulders at 380, 400 and 425 nm (Figure 2a, blue line, and Extended Figure 1a). These spectral features persist across varying concentrations (Extended Figure 1b) and solvent polarities (Extended Figure 1c, solid lines), confirming their locally excited (LE) character. In contrast, excitation at 355 nmresults in a red-shifted, still vibronically structured emission band, with maxima at 384, 404 and 425 nm (Figure 2b, orange line). While this band overlaps with the shoulder features observed under 300 nm excitation, their maxima are not coincident, suggesting they originate from distinct electronic levels, which will subsequently be assigned to $S_0 \leftarrow S_2$ and $S_0 \leftarrow S_1$ transitions, respectively. Furthermore, the vibrational resolution and the absence of a solvatochromic shift across different polarities confirm the LE character of this transition (Extended Figure 1c, dashed lines). Integrated photoluminescence intensity is enhanced 2.4-fold and 3.8-fold for $S_0 \leftarrow S_1$ and $S_0 \leftarrow S_2$ transitions, respectively, upon deaeration, due to the decrease of singlet quenching by oxygen (See SI section 4.1). To elucidate the origin of the dual prompt fluorescence (PF), excitation spectra of the two emission bands were recorded. When monitoring the redder emission (λ_{Em} = 400 nm; Figure 2b), two primary excitation bands emerge at longer wavelengths, with maxima at 351 nm and 378 nm. They are assigned to the S_1 state. Conversely, monitoring emission at 365 nm, the resulting excitation profile shows a sharp cut-off at 350 nm and a primary maximum at 336 nm, effectively excluding excitation from the S_1 state. This divergence in the excitation profiles in dilute solutions provides evidence for an anti-Kasha behavior, where the strong higher-energy emission is assigned to $S_0 \leftarrow S_2$ decay, while the lower-energy emission is identified as the $S_0 \leftarrow S_1$ transition.

To exclude that this dual-PF emission arises from the coexistence of monomeric and dimeric species, an antisolvent experiment was performed in THF-water mixtures with a constant total concentration of 20 μM (Extended Figure 2 and SI section 4.2). The dual-emission remained remarkably unchanged at $f_w \leq 60\%$, indicating a strong THF–**MHTX** interaction that forms a protective solvation shell, effectively hindering molecular aggregation despite the increasing presence of water. In contrast, at $f_w \geq 70\%$, the S_2 emission strongly decreases, and the S_1 emission appears when exciting at 300 nm (into S_2). Exciting into S_1 (355 nm) gives very weak S_1 emission from 0 to 70% water content, followed by a distinct 4 nm (0.03 eV) red-shift of the band at higher water fractions. This coincides perfectly with the emergence of the strong S_1 emission and decline of S_2 emission when exciting at 300 nm. We suggest this is due to the formation of a weak intermolecular dimer as the water content slightly overcomes the stabilizing THF solvation shell, where the molecular orbitals remain predominantly localized on individual molecules. The sustained spectral profile with low to moderate f_w confirms that both the S_2 and S_1 bands are intrinsic to the monomeric species, rather than being products of ground-state association dimer or excimer formation. Both assignments are further supported by the DFT calculations discussed in the following sections. At f_w>50%, an additional band starts to grow 525 nm, attributed to emission from disordered aggregate states, formed as **MHTX** drops out of solution at high water content.

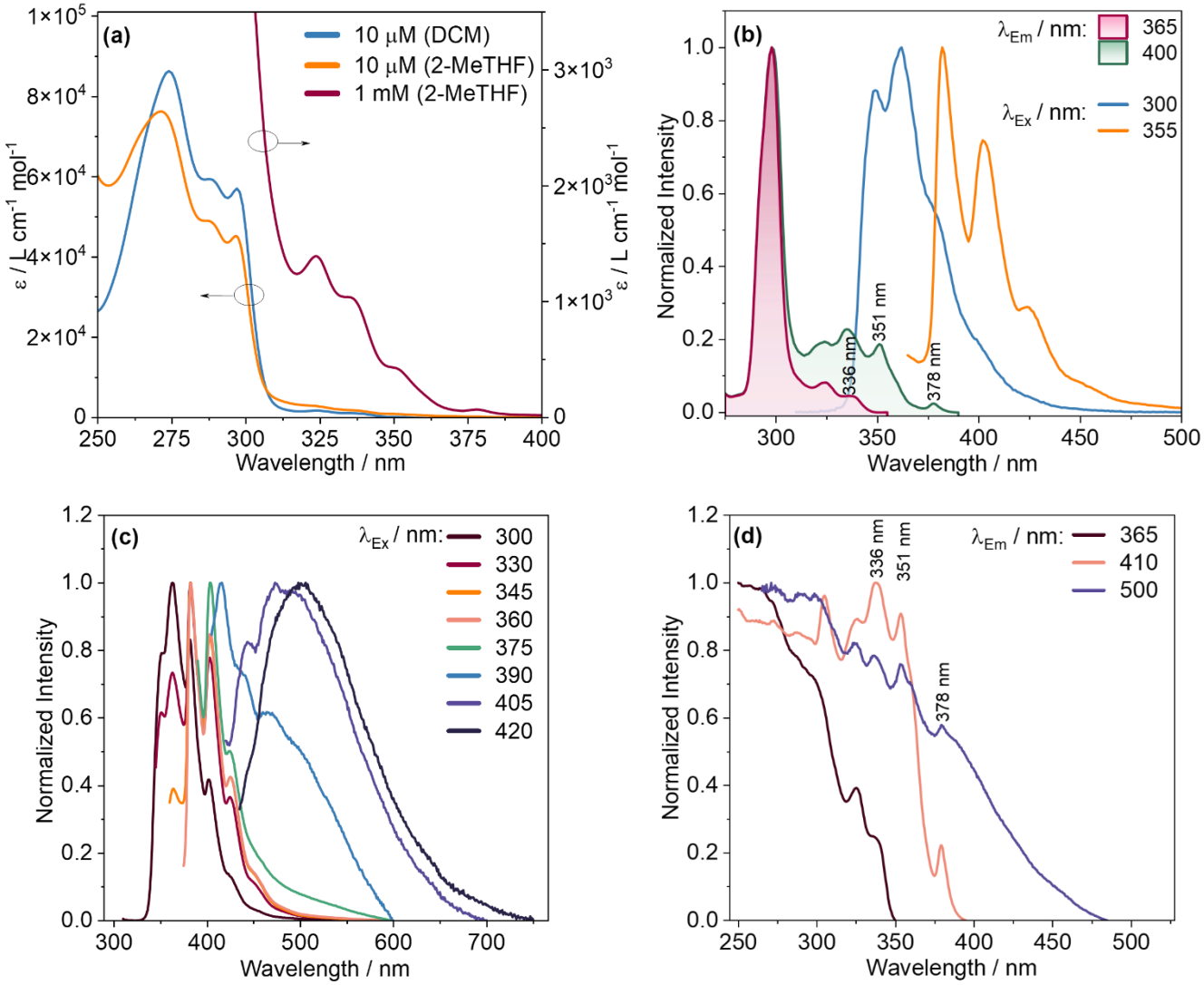


Figure 2. Steady-state photoluminescence and excitation profiles of MHTX at room temperature. (a) Absorption spectra of **MHTX** in 10 μM solutions in DCM (blue) and 2-MeTHF (orange), and 1 mM solution in 2-MeTHF (dark red). **(b)** Normalized excitation and emission spectra in 2-MeTHF (10 μM). **(c)** Normalized emission spectra of a 1 wt.% drop-cast film in Zeonex under different excitation wavelengths in the presence of molecular oxygen. **(d)** Normalized excitation spectra under the same conditions as Figure (c).

The anti-Kasha emission is preserved in the drop-cast film (1 wt.% in Zeonex; Figure 2c and d), showing a marked contrast to previously reported systems where S_2 emission is restricted to solution[31]. In the film, we observe an intensification of the S_1 emission relative to the S_2 band under high-energy excitation (λ_{Ex} = 300 and 330 nm; Figure 2c). This is attributed to the rigidifying effect of the Zeonex matrix, which suppresses large-amplitude molecular vibrations and restricts the non-radiative dissipation prevalent in fluid media. This structural confinement is further supported by the prompt fluorescence lifetime, determined via time-correlated single photon counting (TCSPC) in the solid state (Figure S14), yielding values of 30.6 ns and 42.9 ns for S_2 and S_1. The S_1 decay in the solid state is approximately 10 ns longer than in degassed solution (32.9 ns), while the τ_{PF} for S_2 remains nearly identical (29.7 ns in solution and 30.6 ns in film), confirming the higher sensitivity of S_1 to vibrational suppression by the polymer matrix. Excitation at longer wavelengths (λ_{Ex} = 390, 405 and 420 nm; Figure 2c) leads to a red-shifted, broad emission, dominated by the decay of strongly coupled aggregates, herein called "strong aggregate". The rigidity of **MHTX** minimizes conformational reorganization upon photoexcitation, with small Stokes shifts ($\Delta\nu$) of 0.15 eV and 0.05 eV for the S_2 and S_1 transitions; a spectroscopic signature of constrained geometries. The PLQY of **MHTX** in degassed solution (20 μM in 2-MeTHF) is remarkably higher than that of its analogous structures under identical conditions (λ_{Ex} = 310 and 355 nm): **MHTX** achieves PLQYs of 57% and 32% at these respective wavelengths, significantly outperforming **HTX** (32%/21%) and **TX** (14%/1.8%). This enhancement is attributed to the increased structural rigidity of **MHTX** relative to **HTX** and the breaking of C_{3h}-symmetry relative to **TX**. The latter

effectively mitigates the symmetry-forbidden nature of the $S_1 \rightarrow S_0$ transition, thereby enhancing radiative rates[32–35]. This superior performance extends to the solid state (1 wt.% in Zeonex), where the PLQY reaches 49% (λ_{Ex} = 310 nm) and 63% (λ_{Ex} = 355 nm). **MHTX** significantly outperforms **HTX** (32%, λ_{Ex} = 355 nm) and **TX** (35%, λ_{Ex} = 355 nm) even in the condensed phase, underscoring the efficacy of our molecular design in modulating the excited-state landscape to favor radiative transitions across multiple singlet states.

Dual delayed emissions of MHTX

In addition to the dual PF observed in the UV-to-blue region upon excitation to S_2, **MHTX** displays a distinct blue emission band under vacuum, with vibrational peaks at 452, 485, and 515 nm and a shoulder around 565 nm (Figure 3a). The marked increase in intensity of this emission at 80 K, coupled with its complete quenching under air at room temperature (Figure S15a), suggests a triplet state-mediated mechanism, which we attribute to phosphorescence (Ph) from monomeric species, a feature that is preserved in the neat film (Figure S15b). This blue phosphorescence is consistent with previously reported triplet emissions for **TX** and other truxene-derived compounds[35,36]. In contrast, direct excitation of the S_1 state (λ_{Ex} = 355 nm) yields a very weak, red-shifted orange emission with maxima at 545 and 595 nm, appearing alongside S_1 monomeric PF (Figure 3b). This orange component is attributed to phosphorescence from aggregates, a conclusion substantiated by its higher intensity in the neat film compared to a dilute sample (Figure S15c).

The blue Ph is extremely weak upon S_1 excitation, compared to excitation to S_2 (Figure 3c; λ_{Ex} = 355 and 300 nm, respectively), indicating an inefficient ISC from S_1 due to weak SOC between S_1 and an isoenergetic triplet state. This divergence suggests that S_2 serves as the primary gateway for population of monomeric triplets. To confirm the negligible contribution of S_1 to the monomeric triplet population, excitation spectra were collected at 80 K while monitoring the monomeric phosphorescence at 485 nm (Figure 3d, green shaded) and compared to the S_2 and S_1 excitation profiles (Figure 3d, red and orange shaded). The phosphorescence excitation spectrum excludes the sharp transition regions corresponding to the S_1 state. This selective phosphorescence excitation profile confirms that intersystem crossing is more efficient from the higher-energy S_2 state than from the S_1. Potential indicating that (π,π^*) (σ, π^*) coupling drives the ISC.

Time-gated photoluminescence measurements on a 1 wt.% Zeonex drop-cast film at 80 K confirm the long-lived nature of the cyan emission relative to the PF (λ_{Ex} = 337 nm, Figure 3e). While the PF is observable at early TDs of 1.1 to 122.5 ns, the delayed emission becomes predominant at a delay of 178 μs and persists through the experimental detection limit (40 ms). The phosphorescence spectral profile overlaps with the strongly coupled PF from aggregates centered at approximately 500 nm, in the nanosecond regime. Conversely, excitation to S_1 (λ_{Ex} = 355 nm, Figure 3f) yields the weaker combination of monomeric and aggregate phosphorescence that emerges only after longer TDs (5.6 ms). This kinetic behavior is consistent with the 1 wt.% drop-cast film at room temperature (Figure S18 and Table S3), frozen solution (Figure S19), and neat films at both room temperature and 80 K (Figure S20).

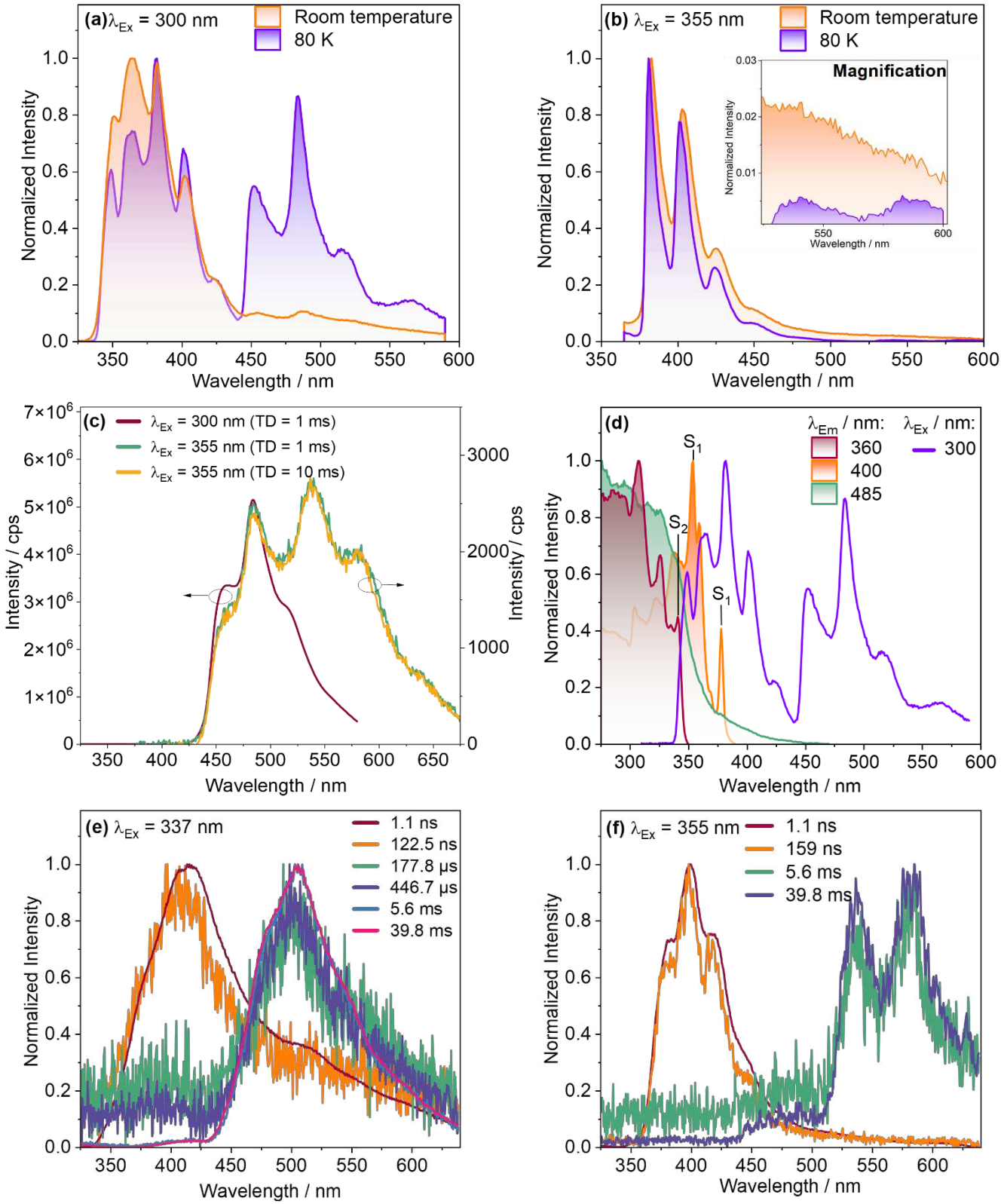


Figure 3. Temperature- and time-dependent photoluminescence of MHTX. (a–b) Normalized steady-state emission of **MHTX** (1 wt.% in Zeonex) at room temperature (orange area) and 80 K (purple area) upon excitation at (a) 300 nm and (b) 355 nm. **(c)** Emission spectra at different time delays upon excitation at 300 nm (red line, left y-axis) and 355 nm (orange and green lines, right y-axis) at 80 K. **(d)** Combined emission and excitation spectra recorded at different emission wavelengths (λ_{Em}), highlighting the exclusion of S_1 vibrational bands (labeled) when monitoring high-energy phosphorescence. **(e–f)** Time-gated emission spectra at 80 K recorded at the indicated time delays following excitation at (e) 337 nm (0.5 wt.% in Zeonex) and (f) 355 nm (0.1 wt.% in Zeonex).

To verify the contribution of TTA to the delayed emissions of **MHTX**, as previously reported for C_3-symmetric **HTX**[24], power-dependent photoluminescence analyses were performed on a drop-cast 1-wt.%-in-Zeonex film under vacuum. At both room temperature and 80 K (Extended Figure 3a–d), the emission intensity exhibits a non-linear dependence on the excitation dose, with a slope of 2 that changes to 1.1 in the high-power regime. This kinetic behavior is characteristic of a bimolecular TTA process[37,38] and confirms that at the early stage,

delayed emission is dominated by TTA-DF within the strong aggregates. In contrast, in frozen dilute solution (Extended Figure 3e–f), the slope was found to be 0.9, indicating the dominance of monomolecular phosphorescence under dilute conditions, where the spatial separation of triplet states precludes the bimolecular interactions required for TTA. A 1 wt.% Zeonex film of **TX** exhibited a consistent power-dependence slope of approximately 1.0 across the entire excitation range at room temperature, confirming that its delayed emission is governed exclusively by long-lived RTP [36] (Figure S21).

The delayed emission of **MHTX** is remarkably long-lived; upon excitation to the S_2 state (λ_{Ex} = 337 nm), a cyan emission remains visible to the naked eye for more than 12 s at room temperature (Figure 4a) and extends to 20 s at 80 K (Figure 4b). To our knowledge, this is the longest blue phosphorescence observed for a hydrocarbon. TCSPC measurements at 80 K with an 11 s time window on the 1 wt.% Zeonex film reveal a biexponential decay (Figure 4c). The primary component (τ_{Ph} > 3.66 s) accounts for 70% of the total emission and is assigned to ultra-long phosphorescence, while the secondary component (τ_{TTA} = 502 ms), contributing 30%, is attributed to TTA-DF. In contrast, the frozen dilute solution (10 µM in 2-MeTHF; Figure 4d) shows a monoexponential decay with τ_{Ph} > 5.0 s. Due to the exceptionally long-lived emission, which prevents the acquisition of a complete decay profile within the experimental window, these lifetime values represent lower-end estimates rather than absolute determinations. The orange aggregate phosphorescence from a powder sample also is long-lived, remaining visible to the naked eye after the UV excitation (λ_{Ex} = 365 nm) is turned off (Figure 4e). This emission persists even in the presence of oxygen, indicating low oxygen permeability of the powder. TCSPC measurements of a 1 wt.% drop-cast film under vacuum at 80 K reveal a lifetime of 98.1 ms for this aggregate emission (Figure 4f). This value is shorter than both the monomeric phosphorescence and the aggregate TTA-DF (τTTA = 502 ms), suggesting efficient triplet-triplet interactions via enhanced triplet migration within the aggregate species.

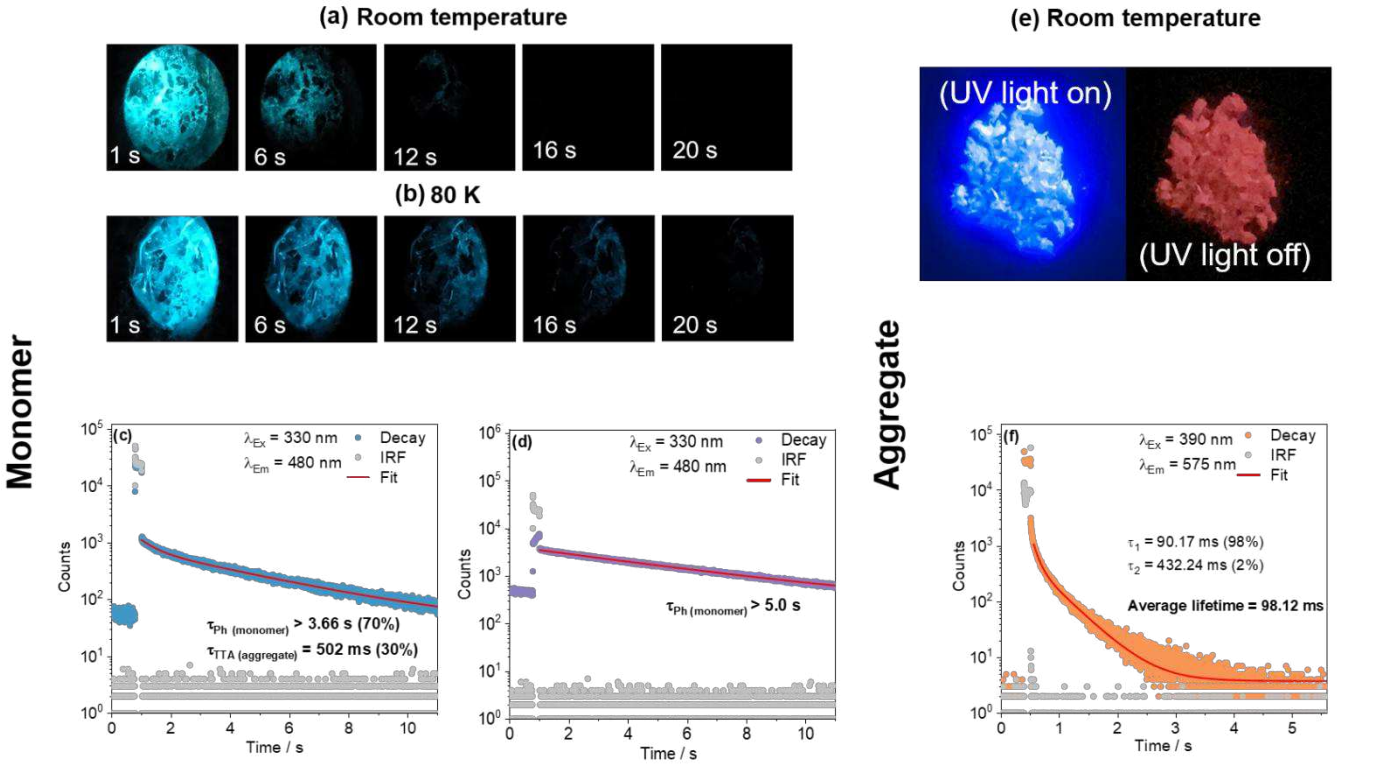


Figure 4. Long-lived luminescence of MHTX. (a–b) Photos showing the persistent cyan luminescence of a film of 1 wt.% **MHTX** in Zeonex after the removal of the excitation source (λ_{Ex} = 337 nm) at **(a)** room temperature and **(b)** 80 K. **(c–d)** Time-resolved luminescence decay profiles recorded via TCSPC (11 s time window) for **(c)** 1 wt.% **MHTX** in Zeonex at 80 K and **(d)** a 10 µM solution of **MHTX** in 2-MeTHF at 80 K (λ_{Ex} = 330 nm, λ_{Em} = 480 nm). The red solid lines are numerical fits and the gray dots are the instrument response function (IRF). **(e)** Photos of **MHTX** powder at room temperature under UV irradiation (λ_{Ex} = 365 nm, left) and after the excitation source is turned off (right), showing the orange luminescence. **(f)** Time-resolved luminescence decay profile of the aggregate emission recorded for 1 wt% **MHTX** in Zeonex (λ_{Ex} = 390 nm, λ_{Em} = 575 nm). The red solid line is the numerical fit and the gray dots are the instrument response function (IRF).

Theoretical Investigations

To confirm the proposed excited states for the many observed emissions, DFT calculations were performed. The geometry of the S_0 state was first optimized to assign the photon absorption states. The calculated UV/Vis absorption spectrum shows that the experimentally observed intense absorption band with a maximum at 271 nm (Figure 2a) corresponds to the $S_0 \rightarrow S_4$, $S_0 \rightarrow S_3$, and $S_0 \rightarrow S_2$ transitions, with large oscillator strengths (f >0.3500, Figure S22 and Table S4). The weak absorption feature between 315 and 355 nm arises from the symmetry-forbidden $S_0 \rightarrow S_1$ transition (f = 0.0012). The low oscillator strength of this transition reflects its symmetry-forbidden character, a behavior also observed in the parent C_3-symmetric **TX**, where the $S_0 \rightarrow S_2$ and $S_0 \rightarrow S_1$ transitions are symmetry-forbidden (f = 0.0000)[36]. This demonstrates that the dissymmetry of **MHTX** allows the weak S_1 transition (see Figure S23 for the molecular orbital degeneracy). Photoexcitation at 355 nm and 300 nm is therefore considered to populate S_1 and S_2, respectively.

The S_1 and S_2 states were geometry-optimized (Figure 5a-b) to investigate the relaxation processes following photon absorption. The calculated fluorescence spectra from S_1 and S_2, which have different electronic wavefunction distributions, reproduce the experimental spectral lineshapes observed for 355 and 300 nm excitations, respectively (Figure 5c), suggesting that the emissions originate from distinct excited electronic states. The calculated spectral wavelengths differ from the experimental values because the excitation energies are overestimated, as is common in DFT calculations. The reorganization energy of $S_0@S_2 \rightarrow S_0@S_0$ (0.27 eV) is larger than that of $S_0@S_1 \rightarrow S_0@S_0$ (0.14 eV). In other words, $S_0@S_2$ exhibits stronger vibronic coupling than $S_0@S_1$, leading to the complex vibronic progression of S_2 fluorescence (Figure S24a-b). The vibrational mode responsible for the vibronic progression of both S_1 and S_2 fluorescence is the C=C stretching vibration with a frequency of around 1650 cm^{-1} (Figure S24c-d). The potential energy curves connecting the S_1 and S_2 geometries show that the S_1/S_2 crossing point is geometrically separated from the S_2 optimized geometry (Figure S25). This spatial separation, together with an activation energy of 0.17 eV, may partially hinder $S_2 \rightarrow S_1$ internal conversion. At the S_1 optimized structure, S_1 and its energetically nearby triplets, particularly T_4, exhibit weak SOC (0.02 cm^{-1}, Figure 5a), reflecting that their electronic wavefunctions are similar (El-Sayed's rule[39]) and show small distribution over the non-planar six-membered ring (Figure S26a). In contrast, the SOC between S_2 and its energetically close T_5 is strong (0.30 cm^{-1}) at the S_2 optimized structure (Figure 5b), attributed to the differences in their wavefunction spatial distributions (Figure S26b). Also, the distribution of the S_2 wavefunction over the non-planar six-membered ring induces the σ and π orbitals mixing, thereby contributing to the strong SOC. These results suggest that S_2 excitation enhances triplet production and therefore phosphorescence, compared to S_1 excitation, through fast ISC from S_2 to triplet states, as shown by the experiments.

To understand the emission from the aggregates, the excited electronic structures of loose and strong dimers were calculated. The loose and strong dimers were modeled using the **MHTX** dimer with and without explicit consideration of 2-MeTHF, respectively (Figure S27a-b). At the S_1 optimized geometry, the presence of 2-MeTHF induces J-type aggregation of **MHTX** with large intermolecular distances. Therefore, the electronic wavefunction is mostly localized on one monomer, with a small distribution on the other, leading to a slight redshift and broadening of the fluorescence spectrum compared to the monomer (Figure 5d and Figure S27c-e). In contrast, in the absence of 2-MeTHF, strong intermolecular interactions cause the dimer to form an excimer with a delocalized electronic wavefunction, resulting in a further red-shifted and broadened fluorescence spectrum (Figure 5d and Fig. S27c-e). Thus, increasing the water fraction in the solvent, as examined by the anti-solvent experiment, promotes the progression from the loose to strong dimer formation.

The T_1 states of the monomer and strong dimer were geometry-optimized to investigate their phosphorescence properties. For the monomer, T_1 exhibits a strong SOC with S_3 (0.58 cm^{-1}) which has a large oscillator strength (f = 0.8650, Figure S28a-b). Therefore, phosphorescence from T_1 is considered to occur via intensity borrowing from the S_3-S_0 transition dipole moment. The calculated phosphorescence spectrum reproduces the experimental spectral lineshape observed on 355 nm excitation (Figure S28c). The reorganization energy of $S_0@T_1 \rightarrow S_0@S_0$ is 0.33 eV. $S_0@T_1$ provides strong vibronic coupling for several vibrational modes,

particularly the C=C stretching mode with a frequency of 1559 cm^{-1} (Figure S28d), resulting in intricate vibronic spectral patterns. For the strong dimer, the electronic wavefunction is primarily localized on one monomer, with slight delocalization onto the other (Figure S28e-f), suggesting that the phosphorescence from the aggregate resembles that from the monomer.

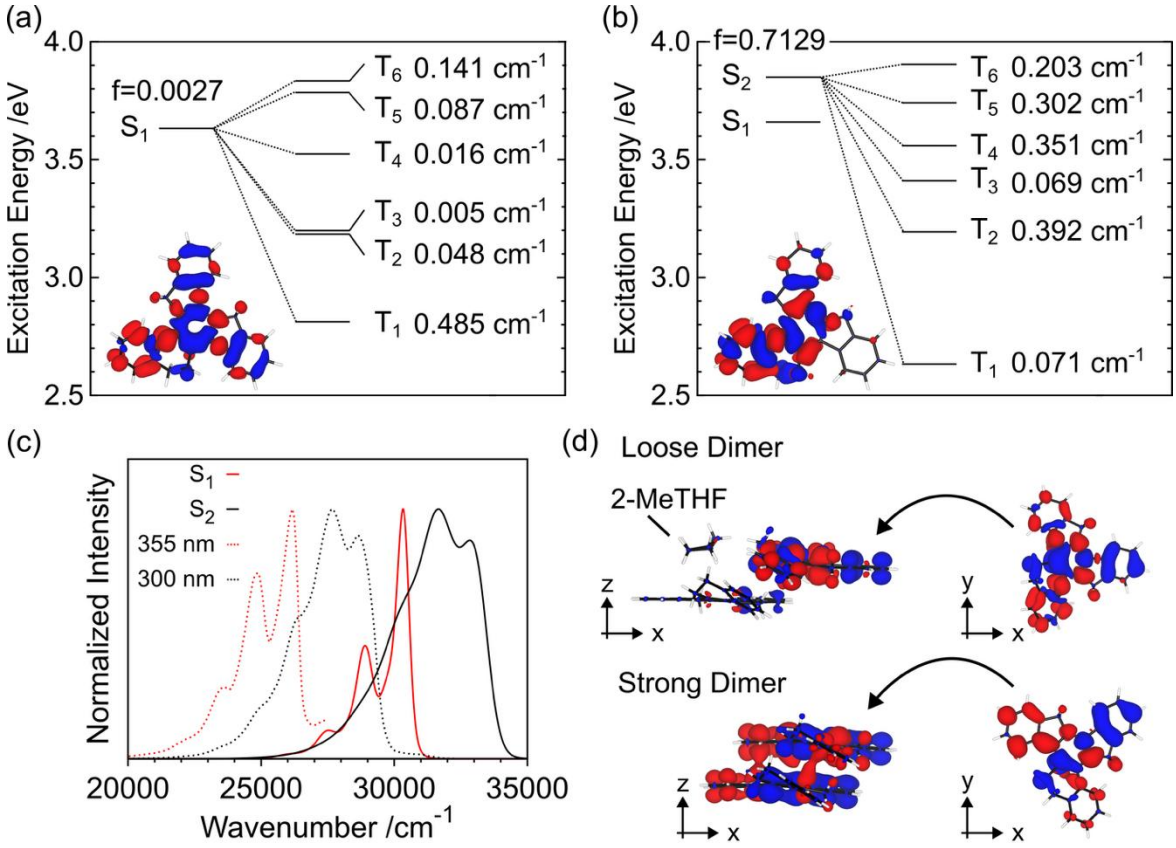


Figure 5. Theoretical calculation on the monomeric and aggregated properties of MHTX. Energy levels of excited states at the **(a)** S_1 and **(b)** S_2 optimized structures. Inset shows the electron density difference of S_1-S_0 and S_2-S_0 (isosurface value: 5×10^{-4} a.u.). Red and blue regions indicate positive and negative values. Values represent the SOC matrix element between singlets and triplets. *f* represents the oscillator strength of S_1-S_0 and S_2-S_0. **(c)** Calculated S_1 and S_2 fluorescence spectra (solid lines), compared with the experimental spectra under 355 nm and 300 nm excitations (Fig. 2b). The density of final vibronic states is expressed using the Gaussian function with a linewidth of 100 cm^{-1}. **(d)** Electron density difference between S_1 and S_0 at the S_0 optimized structure for the loose and strong dimers (isosurface value: 5×10^{-4} a.u.).

Discussion

The observation of dual ultra-long delayed emissions, visible to the naked eye, from a small non-symmetric twisted hydrocarbon represents a remarkable achievement in molecular photophysics. This underscores the effectiveness of our molecular design in promoting three key outcomes: the formation of dual-emissive species (monomers and aggregates), efficient triplet harvesting, and exceptionally long-lived emissions. The decay mechanisms for the multiple emissions of **MHTX** are summarized in Figure 6. Upon excitation to the S_2 state, the monomeric species preferentially emit directly from the S_2 level at 350 nm, in a clear example of anti-Kasha prompt fluorescence. The fraction that effectively relaxes to S_1 emits at 384 nm. The PLQY on exciting into S_2 is much higher than that from exciting into S_1, indicating slow IC from $S_2 \rightarrow S_1$. Concurrently, spin-orbit coupling facilitates intersystem crossing from S_2 to T_5, which subsequently populates the long-lived monomeric T_1 state via fast internal conversion between the triplet states. This process leads to a combination of TTA from aggregates and long-lived delayed RTP at 484 nm. On the other hand, direct monomeric S_1 excitation yields weak monomeric and predominant aggregate phosphorescence due to poor spin-orbit coupling between S_1 and its isoenergetic triplet state.

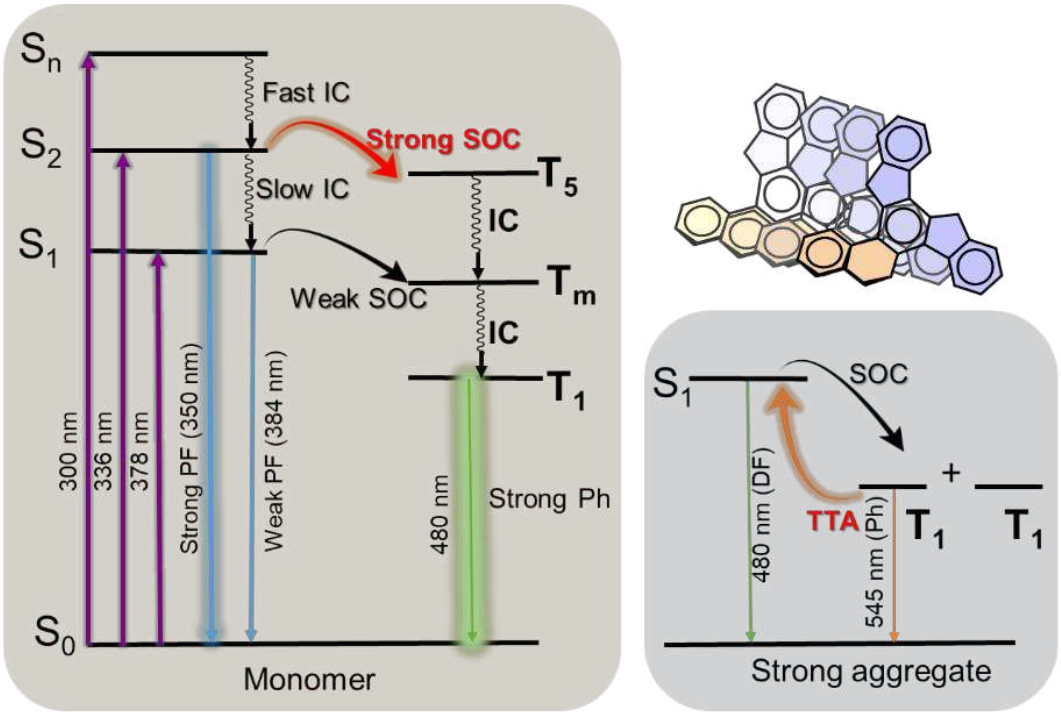


Figure 6. Summary of the excited-state mechanisms of MHTX. Simplified Jablonski diagram summarizing the rich photophysics of monomeric and aggregate species of **MHTX**.

Conclusions

In summary, we have demonstrated that reducing the structural symmetry of a homotruxene core from three twisted arms to one in monohomotruxene maintained the complex photophysical properties of **HTX** gave a significant enhancement of photoluminescence quantum yields and phosphorescence lifetimes. The photophysical behavior of **MHTX** is remarkably rich and characterized by a strong violation of Kasha's rule due to an inefficient internal conversion between S_2 and S_1 states. In addition, upon excitation to the S_2 state, the monomeric species phosphoresces in the cyan-colored spectral region, where an efficient intersystem crossing from an upper excited state ($S_2 \rightarrow T_5$) leads to an ultralong-lived high-energy triplet state. This results in intense phosphorescence, visible to the naked-eye persisting for over 12 seconds at room temperature (298 K) and 20 s at 80 K. Conversely, excitation to the S_1 state selectively probes the S_1 prompt fluorescence monomeric emission and TTA in the neat film. Aggregate species of **MHTX** phosphoresces in the orange region and emits by TTA in the cyan region. Overall, this work establishes the non-symmetric monohomotruxene core as a highly promising scaffold. The insights gained into its complex, tunable decay pathways provide a fundamental blueprint for the development of new non-symmetric PAHs with tailored optoelectronic properties.

Methods

Photophysical measurements

Absorption spectra in solution were recorded on a Shimadzu 2600i spectrophotometer. Steady-state spectra were acquired for solutions (aerated and degassed) and drop-cast films using Jobin Yvon Horiba Fluorolog and Fluoromax spectrofluorimeters. For low-temperature measurements, a liquid nitrogen cryostat (Janis Research), equipped with optical windows, was used. All solutions were prepared immediately before measurement from the solid compound. Degassed solutions were prepared in a sealed quartz cuvette (equipped with a screw cap and silicon septum) by purging with argon for 10 minutes through a needle. The dispersed drop-cast films were fabricated from blended chloroform solutions of **MHTX** (0.5 mg/mL) and Zeonex® (100 mg/mL) at various ratios. A 100 µL aliquot of the mixture was deposited onto a quartz substrate, and the film was formed by solvent evaporation at 40 °C on a heating plate. Neat films were prepared by depositing

100 μL of the chloroform solution of **MHTX** (0.5 mg/mL) directly onto the quartz substrate, followed by solvent evaporation at 40 ºC.

Time-resolved photoluminescence spectra were measured using pulse excitation (10 Hz) from both a Nd:YAG laser, with excitation wavelength at 355 nm, pulse length 150 ps (SL312, EKSPLA), and from a Nitrogen laser with excitation wavelength at 337 nm. Emission is captured by a sensitive gated intensified charge-coupled device (iCCD) camera from Stanford Computer Optics 4Picos gated intensified CCD camera, with a temporal resolution of 200 ps. Emission decays were constructed by varying the CCD gate delay time relative to the laser trigger and monitoring the change in the integrated spectral area (normalized by the gate time). Time delays (TDs) ranged from 1.1 ns to 39.8 ms. Decay curves were collected by time-correlated single photon counting (TCSPC) with a Horiba DeltaFlex system and Horiba DeltaDiode (405 nm) and SpectraLED (330 nm) as excitation sources. The quantum yields were determined both in thin films and solutions using a Hamamatsu Photonics Absolute Quantum Yield Measurement System model c9920–02G with an integrating sphere, upon excitation at 310 and 355 nm.

Theoretical Calculations

DFT calculations were performed at the B3LYP/6-31G(d,p) level for the ground state and TD-B3LYP/6-31G(d,p) within the Tamm-Dancoff approximation for the excited states. For the dimer calculations, dispersion correction was applied using the DFT-D3 method with Becke-Johnson damping. The solvent effect of 2-MeTHF was included through the polarizable continuum model (PCM) with a static dielectric constant of 6.97 and an optical dielectric constant of 1.98. The above calculations were performed using Gaussian 16 Rev. C02[40]. The spin-orbit coupling (SOC) constants between excited states were computed using Multiwfn[41]. The emission spectrum, accounting for all vibrational modes, was computed within the displaced harmonic oscillator approximation[42,43]. For S_1 and S_2 fluorescence of the monomer and S_1 fluorescence of the dimer, the displacement vector between the initial (S_1 or S_2) and final (S_0) electronic states was determined within the crude adiabatic approximation using the energy gradient of the final state at the equilibrium geometry of the initial state[44]. In contrast, for T_1 phosphorescence of the monomer, the displacement vector was obtained within the Born-Oppenheimer approximation due to the substantial structural reorganization[45].

Acknowledgements

The authors are grateful for financial support from the European Union (Horizon-MSCA #101182946 GHOST) and INCT/INEO (FAPESP process #2025/ 27044-5), as well as CAPES (finance code #937-20 and #001), COFECUB (joint project Ph-C 962/20), CNPq and FAPESC (2024TR002240). This work was also supported by JSPS KAKENHI Grant Number JP24K23082. Numerical calculations were performed using the ACCMS supercomputer at Kyoto University. CF thanks the University of Durham for her PhD studentship.

Contributions

H.B. conceived the molecular structure. M.S.K. performed the synthesis of **MHTX**. M.S.K. and M.S.C. did the optimization of the synthetic route. D.C. and I.H.B. performed the photophysical characterization in the powder state. M.S.K. and C.F. did the photophysical characterization of solutions and guest-host films. E.F. and W.O. performed the theoretical calculations. T.S., I.H.B., W.O., A.P.M., E.W. and H.B. directed and supervised the study. All authors analyzed and discussed the data. M.S.K. wrote the manuscript and C.F. edited the manuscript with input from all authors.

References

1. Wu, Z., Nitsch, J. & Marder, T. B. Persistent Room-Temperature Phosphorescence from Purely Organic Molecules and Multi-Component Systems. *Adv. Opt. Mater.* **9**, 2100411 (2021).
2. Luo, X. *et al.* Room-temperature phosphorescent materials derived from natural resources. *Nat. Rev. Chem.* **7**, 800–812 (2023).
3. She, P. *et al.* Lifetime-tunable organic persistent room-temperature phosphorescent salts for large-area security printing. *Sci. China Mater.* **64**, 1485–1494 (2021).
4. Shi, L., Ding, L., Zhang, Y. & Lu, S. Application of room-temperature phosphorescent carbon dots in information encryption and anti-counterfeiting. *Nano Today* **55**, 102200 (2024).
5. Stanitska, M., Volyniuk, D., Minaev, B., Agren, H. & Grazulevicius, J. V. Molecular design, synthesis, properties, and applications of organic triplet emitters exhibiting blue, green, red and white room-temperature phosphorescence. *J. Mater. Chem. C Mater.* **12**, 2662–2698 (2024).
6. Zhang, G., Palmer, G. M., Dewhirst, M. W. & Fraser, C. L. A dual-emissive-materials design concept enables tumour hypoxia imaging. *Nat. Mater.* **8**, 747–751 (2009).
7. Cong, Z. *et al.* Ultralong blue room-temperature phosphorescence by cycloalkyl engineering. *Mater. Chem. Front.* **6**, 1606–1614 (2022).
8. Hamzehpoor, E. *et al.* Efficient room-temperature phosphorescence of covalent organic frameworks through covalent halogen doping. *Nat. Chem.* **15**, 83–90 (2022).
9. Yam, V. W. W., Chan, A. K. W. & Hong, E. Y. H. Charge-transfer processes in metal complexes enable luminescence and memory functions. *Nat. Rev. Chem.* **4**, 528–541 (2020).
10. Kwon, M. S. *et al.* Suppressing molecular motions for enhanced room-temperature phosphorescence of metal-free organic materials. *Nat. Comm.* **6**, 8947- (2015).
11. Shao, W. & Kim, J. Metal-Free Organic Phosphors toward Fast and Efficient Room-Temperature Phosphorescence. *Acc. Chem. Res.* **55**, 1573–1585 (2022).
12. Wang, Y. *et al.* Metal-Free organic polymeric room temperature phosphorescence system with Multi-Colour and ultralong lifetime. *Chem. Eng. J.* **481**, 148642 (2024).
13. Hakkarainen, E. *et al.* Metal-free pyridinium salts with strong room-temperature phosphorescence and microsecond radiative lifetime. *Chem. Sci.* **16**, 17261–17267 (2025).
14. Zhao, W., He, Z. & Tang, B. Z. Room-temperature phosphorescence from organic aggregates. *Nat. Rev. Mater.* **5**, 869–885 (2020).
15. Lai, L., Fang, B., Fan, M., Cheng, W. & Yin, M. Modulating Room-Temperature Phosphorescence through the Synergistic Effect of Heavy-Atom Effect and Halogen Bonding. *J. Phys. Chem. C* **125**, 16350–16357 (2021).
16. Farias, G. *et al.* Halogenation of a twisted non-polar π-system as a tool to modulate phosphorescence at room temperature. *Chem. Sci.* **12**, 15116–15127 (2021).
17. Dai, W. *et al.* Halogen Bonding: A New Platform for Achieving Multi-Stimuli-Responsive Persistent Phosphorescence. *Angew. Chem. Int. Ed.* **61**, e202200236 (2022).
18. Hirata, S. & Kamatsuki, T. Role of Carbonyl Distortions Facilitating Persistent Room-Temperature Phosphorescence. *J. Phys. Chem. C* **127**, 3861–3871 (2023).

19. Kumar, R., Aggarwal, H. & Srivastava, A. Of Twists and Curves: Electronics, Photophysics, and Upcoming Applications of Non-Planar Conjugated Organic Molecules. *Chem. Eur. J.* **26**, 10653–10675 (2020).

20. Nagarajan, K., Mallia, A. R., Muraleedharan, K. & Hariharan, M. Enhanced intersystem crossing in core-twisted aromatics. *Chem. Sci.* **8**, 1776–1782 (2017).

21. Wu, B. *et al.* The El-Sayed's rule analogy enables long-lived room temperature phosphorescence in twisted biphenyls. *Cell Rep. Phys. Sci.* **4**, 101245 (2023).

22. Liao, C. *et al.* Spin–Vibronic Coupling Enhanced Intersystem Crossing beyond El-Sayed Restrictions. *J. Am. Chem. Soc.* **147**, 22176–22184 (2025).

23. Hirata, S. Molecular physics of persistent room temperature phosphorescence and long-lived triplet excitons. *Appl. Phys. Rev.* **9**, (2022).

24. Salla, C. A. M. *et al.* Persistent Solid-State Phosphorescence and Delayed Fluorescence at Room Temperature by a Twisted Hydrocarbon. *Angew. Chem. Int. Ed.* **58**, 6982–6986 (2019).

25. El-Sayed, M. A., Moomaw, W. R. & Chodak, J. B. The mechanism of the S1 ⇝ Tx intersystem crossing process in aromatic hydrocarbons from PMDR. *Chem. Phys. Lett.* **20**, 11–16 (1973).

26. Pyrko, A. Self-condensation of 6-Methoxytetralone. *ChemInform* **23**, (1992).

27. Amick, A. W. & Scott, L. T. Trisannulated Benzene Derivatives by Acid Catalyzed Aldol Cyclotrimerizations of Cyclic Ketones. Methodology Development and Mechanistic Insight. *J. Org. Chem.* **72**, 3412–3418 (2007).

28. Guo, Y. *et al.* Stepwise deprotonation of truxene: structures, metal complexation, and charge-dependent optical properties. *Chem. Sci.* **14**, 13219–13227 (2023).

29. Kaur, B., Moghe, D., Dey, A., Kabra, D. & Jacob, J. Solution processable truxene based blue emitters: Synthesis, characterization and electroluminescence studies. *J. Lumin.* **196**, 511–519 (2018).

30. Nakajima, A. Fluorescence Emission in the Gas Phase of Several Aromatic Hydrocarbons. *Bull. Chem. Soc. Jpn.* **45**, 1687–1695 (1972).

31. Zhang, X. *et al.* Anomalous anti-Kasha excited-state luminescence from symmetry-breaking heterogeneous carbon bisnanohoops. *Nat. Comm.* **15**, 2684- (2024).

32. Ruiz, C. *et al.* Symmetry Lowering in Triindoles: Impact on the Electronic and Photophysical Properties. *J. Phys. Chem. C* **118**, 5470–5477 (2014).

33. Chen, J. H., Wang, S. A., Liu, Y. H. & Wong, K. T. Synthesis and properties of novel C3-symmetric coplanar chromophores. *Org. Lett.* **13**, 4168–4171 (2011).

34. Kao, M. T. *et al.* Facile synthesis of 5,10,15-hexaaryl truxenes: Structure and properties. *Org. Lett.* **13**, 1714–1717 (2011).

35. Ogaki, T. *et al.* Intramolecular Triple Cyclization Strategy for Sila- and Oxa-Analogues of Truxene with Long-Lived Phosphorescence. *Asian J. Org. Chem.* **6**, 290–296 (2017).

36. Baunsgaard, D. *et al.* Vibronic Activity in the Phosphorescence Spectra of Disklike Aromatic Molecules: A Combined Experimental and Theoretical Investigation. *J. Phys. Chem. A* **102**, 10007–10016 (1998).

37. Dias, F. B., Penfold, T. J. & Monkman, A. P. Photophysics of thermally activated delayed fluorescence molecules. *Methods Appl. Fluoresc.* **5**, 012001 (2017).

38. Dias, F. B. Kinetics of thermal-assisted delayed fluorescence in blue organic emitters with large singlet-triplet energy gap. *Philos. Trans. R. Soc. A* **373**, (2015).

39. El-Sayed, M. A. & Chem Phys, J. Spin—Orbit Coupling and the Radiationless Processes in Nitrogen Heterocyclics. *J. Chem. Phys.* **38**, 2834–2838 (1963).

40. Frisch, M. J. et al. Gaussian 16 Revision C.01. (2016).

41. Lu, T. & Chen, F. Multiwfn: A multifunctional wavefunction analyzer. *J. Comput. Chem.* **33**, 580–592 (2012).

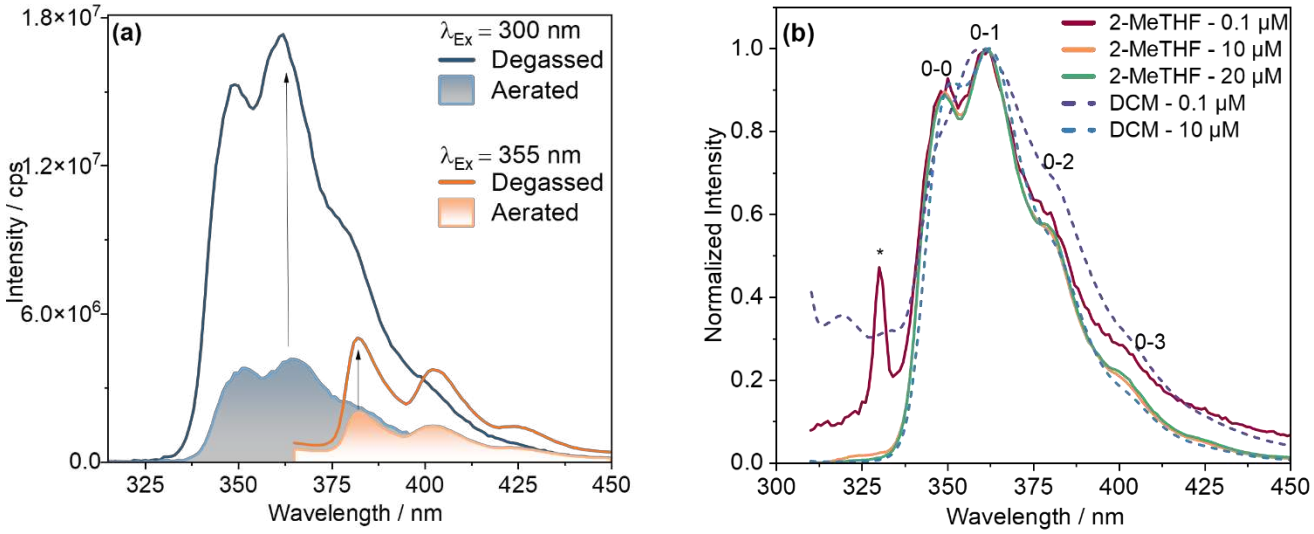
42. Ota, W., Uejima, M. & Sato, T. Role of Vibronic Couplings and Energy Gap in the Internal Conversion Process of a Molecule. *Bull. Chem. Soc. Jpn.* **96**, 582–590 (2023).

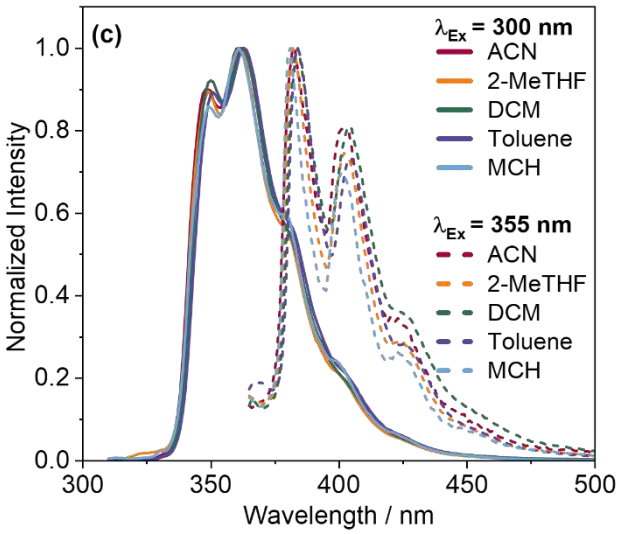
43. Ota, W., Uejima, M., Haruta, N. & Sato, T. Intersystem crossing as vibronically induced phonon emission and absorption processes: a unified view of nonradiative transitions in a molecule. *Bull. Chem. Soc. Jpn.* **97**, (2024).

44. Uejima, M., Sato, T., Yokoyama, D., Tanaka, K. & Park, J. W. Quantum yield in blue-emitting anthracene derivatives: vibronic coupling density and transition dipole moment density. *Phys. Chem. Chem. Phys.* **16**, 14244–14256 (2014).

45. Santoro, F., Improta, R., Lami, A., Bloino, J. & Barone, V. Effective method to compute Franck-Condon integrals for optical spectra of large molecules in solution. *J. Chem. Phys.* **126**, (2007).

Extended Data



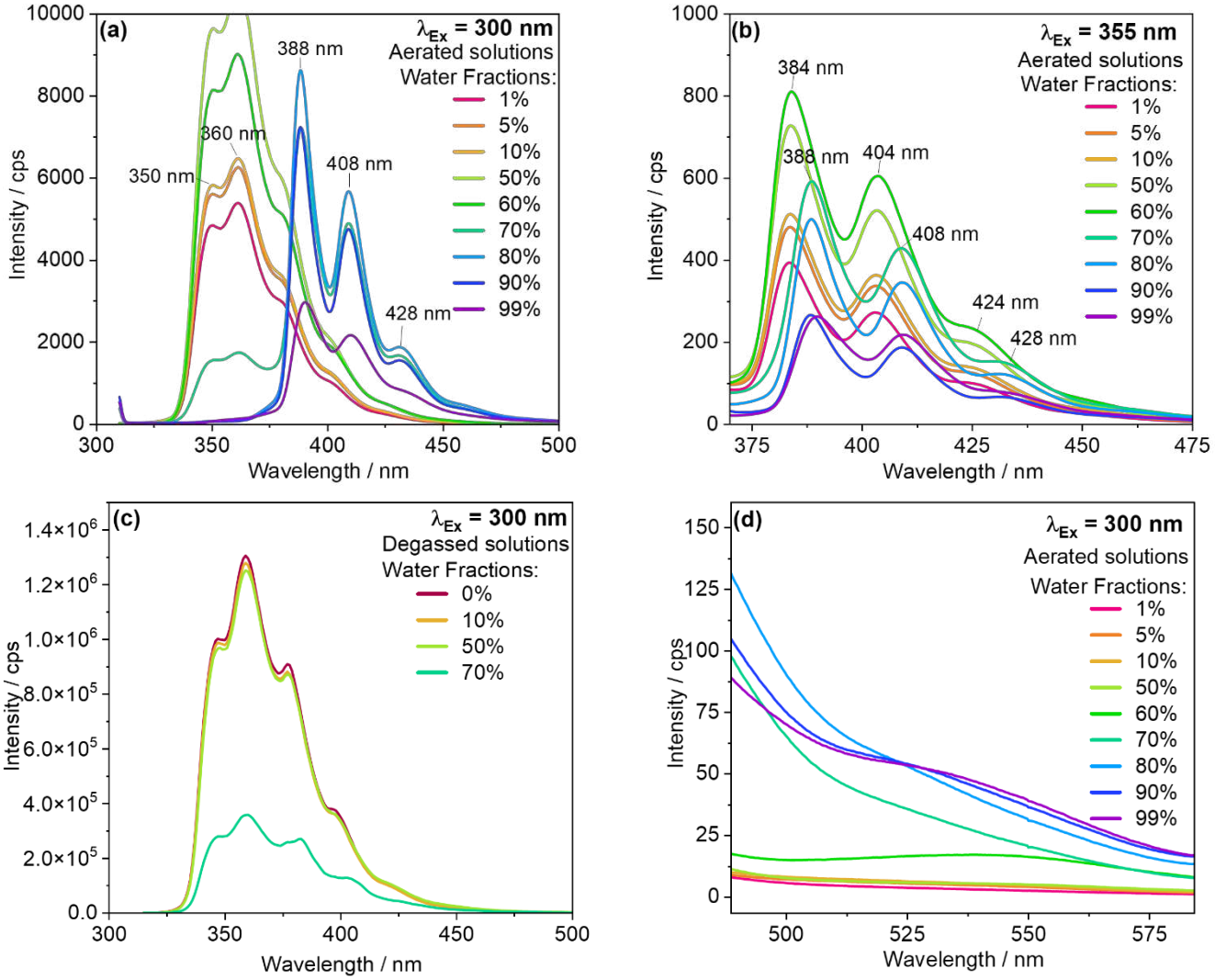


Extended Data Figure 1. Photophysical properties of MHTX as a function of environment and concentration. (a) **Monomeric dual emission and sensitivity to molecular oxygen**. Steady-state emission spectra of **MHTX** (10 μM in 2-MeTHF) at 298 K under aerated (shaded) and degassed (solid lines) conditions. Selective excitation at λ_{Ex} = 300 nm (blue) and 355 nm (orange) reveals intensity enhancement (indicated by arrows) upon deaeration for both S_2 and S_1 manifolds. (b) **Concentration- and solvent-dependent emission profiles**. Normalized emission spectra in 2-MeTHF (solid lines) and DCM (dashed lines) across a range of concentrations. Vibronic progressions (0 → ν') are labeled for the monomeric bands. The emergence of lower-energy features at high concentrations indicates the onset of intermolecular coupling. Asterisk (*) denote solvent Raman scattering. **(c) Solvent-dependent spectral shifts (solvatochromism).** Normalized emission spectra of **MHTX** (10 μM) in solvents of varying polarity upon excitation at λ_{Ex} = 300 nm (solid lines) and 355 nm (dashed lines). MCH, methylcyclohexane; ACN, acetonitrile.

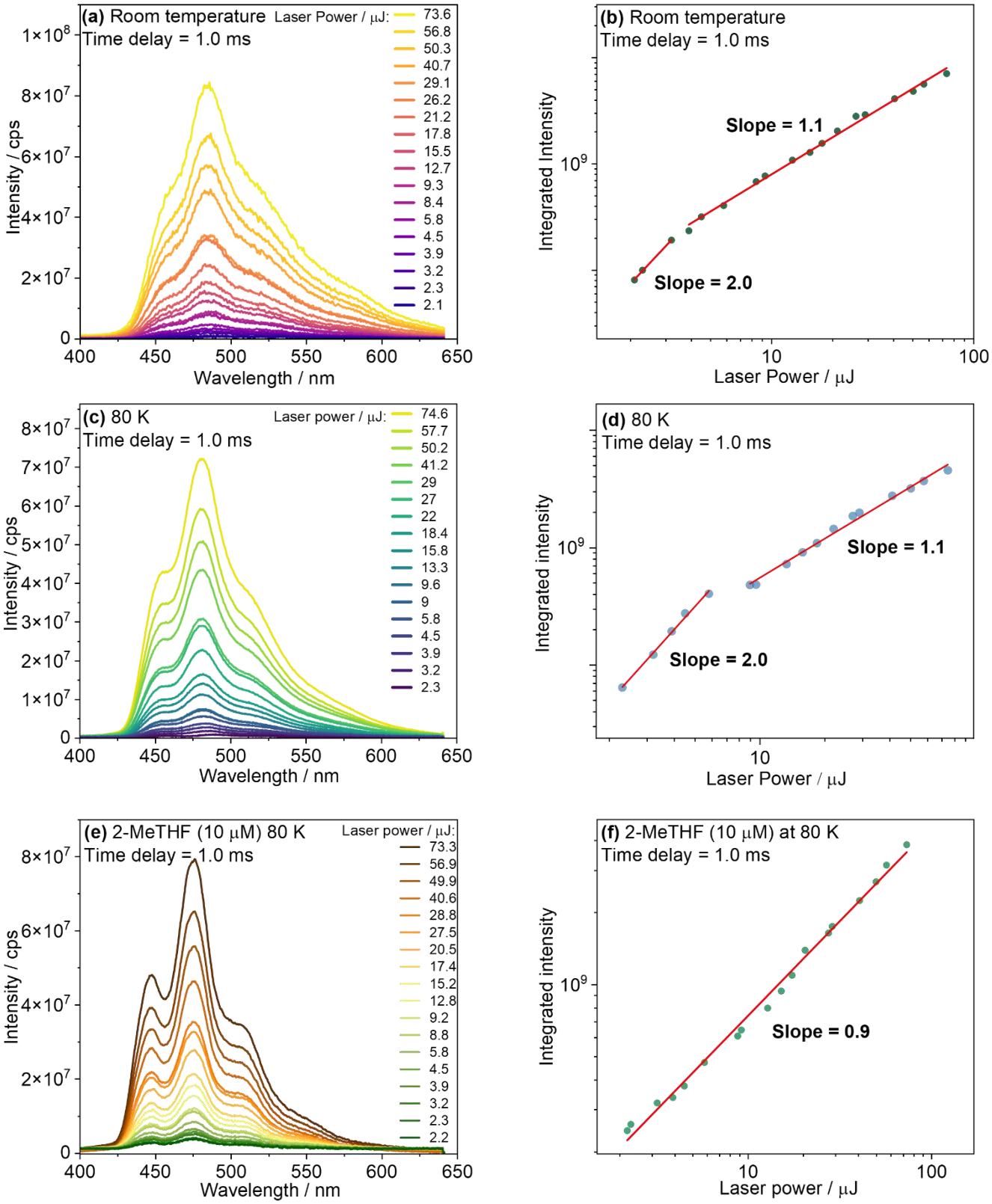
Extended Data Table 1. Steady-state photophysical properties of **MHTX** in solution and solid-state environments.

Conditions	λ_{AB} / nm ($\varepsilon \times 10^4$ / L cm^{-1} mol^{-1})	λ_{Em} (S_1)[a] / nm	λ_{Em} (S_2)[b] / nm	Stokes shift ($\Delta\nu$)[c] / eV	PLQY[d]
Solution	271 (7.6) 288 (4.9) 297 (4.5) 325 (0.14) 336 (0.1) 353 (0.04) 379 (0.006)	350, 360, 380, 400, 425	384, 404, 425	0.15 (S_2) 0.05 (S_1)	57% (310 nm) and 32% (355 nm)
1 wt.% Zeonex film	325, 336, 353. 379	350, 360	384, 404, 425	0.15 (S_2) 0.05 (S_1)	49% (310 nm) and 63% (355 nm)

[a] and [b] Excited at 300 nm and 355 nm, respectively. Data related to the absorption spectrum of a dilute solution in 2-MeTHF (10 μM). [c] Estimated from the wavelengths of the longest λ_{AB} and the shortest λ_{PF} from each decay state, as indicated in parentheses. [d] Absolute quantum yield determined by using an integrating sphere system, upon excitation at 310 nm and 355 nm (degassed 20 μM in 2-MeTHF).



Extended Data Figure 2. Effect of water content of the photophysics of MHTX. Steady-state photoluminescence and excitation spectra of **MHTX** in THF/water mixtures with varying water fractions (f_w) maintaining a constant total concentration of 20 μM. **(a)** PL spectra (λ_{Ex} = 300 nm) showing the stability of the dual S_2 emission profile up to f_w = 60%. **(b)** Emission spectra (λ_{Ex} = 355 nm) selectively exciting the S_1 state. **(c)** Emission spectra (λ_{Ex} = 300 nm) in degassed solutions, highlighting the intensity enhancement upon oxygen removal. **(d)** PL spectra (λ_{Ex} = 300 nm) showing the emission band from a low-energy aggregate at f_w>50%.



Extended Data Figure 3. Time-resolved photoluminescence spectra (left column) and power-dependent plots (right column) of **MHTX** under vacuum (λ_{Ex} = 337 nm) and different conditions: **(a)** and **(b)** measurement at 298 K for a 1 wt.% Zeonex drop-cast film; **(c)** and **(d)** at 80 K for a 1 wt.% Zeonex drop-cast film. **(e)** and **(f)** at 80 K for a 10 µM solution in 2-MeTHF. The time-resolved spectra were collected with a time delay (TD) of 1.0 ms and an integration window of 10 ms.

Supplementary Files

This is a list of supplementary files associated with this preprint. Click to download.

- SIMHTXFINAL2605.pdf